

Global Air Pollution Crossroads over the Mediterranean

J. Lelieveld,^{1*} H. Berresheim,² S. Borrmann,^{1,3} P. J. Crutzen,^{1,4} F. J. Dentener,⁵ H. Fischer,¹ J. Feichter,⁶ P. J. Flatau,^{4,7} J. Heland,⁸ R. Holzinger,¹ R. Korrman,¹ M. G. Lawrence,¹ Z. Levin,⁹ K. M. Markowicz,^{4,10} N. Mihalopoulos,¹¹ A. Minikin,⁸ V. Ramanathan,⁴ M. de Reus,¹ G. J. Roelofs,¹² H. A. Scheeren,¹² J. Sciare,¹³ H. Schlager,⁸ M. Schultz,⁶ P. Siegmund,¹⁴ B. Steil,¹ E. G. Stephanou,¹¹ P. Stier,⁶ M. Traub,¹ C. Warneke,¹⁵ J. Williams,¹ H. Ziereis⁸

The Mediterranean Intensive Oxidant Study, performed in the summer of 2001, uncovered air pollution layers from the surface to an altitude of 15 kilometers. In the boundary layer, air pollution standards are exceeded throughout the region, caused by West and East European pollution from the north. Aerosol particles also reduce solar radiation penetration to the surface, which can suppress precipitation. In the middle troposphere, Asian and to a lesser extent North American pollution is transported from the west. Additional Asian pollution from the east, transported from the monsoon in the upper troposphere, crosses the Mediterranean tropopause, which pollutes the lower stratosphere at middle latitudes.

The summertime Mediterranean basin is directly under the descending branch of the Hadley circulation, driven by deep convection in the Inter-Tropical Convergence Zone. Subsidence over the Mediterranean causes drought, affecting ecosystems, agriculture, and drinking water supplies (1, 2). Owing to cloud-free conditions and high solar radiation intensity, the region is particularly sensitive to air pollution (3, 4). Atmospheric chemistry transport model simulations suggest that summertime ozone (O₃) is enhanced in the entire Mediterranean troposphere, contributing substantially to the radiative forcing of

climate (5–7). Furthermore, several studies indicate that aerosol radiative forcing is among the highest in the world over the summertime Mediterranean (8–10). This provided the rationale to conduct the Mediterranean Intensive Oxidant Study (MINOS) in August 2001 and investigate anthropogenic contributions to these environmental stresses. The coastal measurement station Finokalia in the north of Crete (35°N, 25°E, 70 km east of Heraklion) was used to measure gases, aerosols, radiation, and meteorological parameters. Two aircraft, a German Falcon twinjet (14 flights) and an Israeli King Air (7 flights), were operated from Heraklion airport to perform measurements across the Mediterranean up to an altitude of about 13 km (11).

Air mass trajectories. In summer, a strong east–west surface pressure difference (>20 hPa) is generated between the Azorean high and Asian monsoon low-pressure regimes. These quasi-permanent weather systems cause northerly flow in the lower troposphere over the Mediterranean, feeding into the trade winds further south. The flow is strongest and most persistent in August. In the free troposphere, on the other hand, westerly wind prevails. In the upper troposphere over the eastern Mediterranean, the flow is additionally influenced by the extended anticyclone centered over the Tibetan Plateau. Mean air mass trajectories during MINOS were derived from meteorological data of the European Centre for Medium-range Weather Forecasts (ECMWF) (Fig. 1). The trajectories, which extend over about 3 days, characterize the boundary layer and the lower free troposphere up to about 4 km altitude, the

middle troposphere at about 4 to 8 km, and the upper troposphere at about 8 to 12 km.

Lower and upper tropospheric pollution. Concentrations of important trace gases and aerosols (Fig. 2) are typically factors of 2 to 10 higher over the Mediterranean than in the hemispheric background troposphere; for example, over the North Pacific Ocean in summer (Table 1). We used the North Pacific for comparison because it is expected to be the least polluted environment at low northern latitudes. Throughout the Mediterranean troposphere, formaldehyde (HCHO) mixing ratios are remarkably high. Acetone (CH₃COCH₃) and methanol (CH₃OH) mixing ratios are also high, indicating large in situ production of peroxy radicals. In combination with relatively high nitric oxide (NO) mixing ratios in the upper troposphere, typically 0.1 to 0.2 parts per billion by volume (ppbv), net photochemical O₃ production is about 2 ppbv/day. In addition, O₃ transport from the stratosphere can take place by cut-off lows and tropopause foldings from about

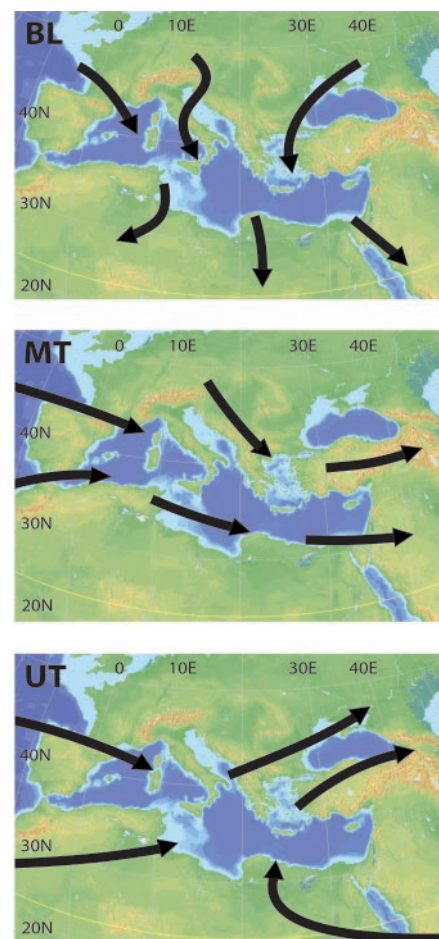


Fig. 1. Schematic air mass trajectories during the MINOS campaign, representing transport during approximately 3 days in the lower, middle, and upper troposphere (from top to bottom, respectively). BL, boundary layer; MT, middle troposphere; UT, upper troposphere.

¹Max Planck Institute for Chemistry, Post Office Box 3060, 55020 Mainz, Germany. ²German Weather Service, Meteorological Observatory, 82383 Hohenpeisenberg, Germany. ³Institute for Atmospheric Physics, University of Mainz, 55099 Mainz, Germany. ⁴Scripps Institution of Oceanography, University of California, San Diego, CA 92093–0221, USA. ⁵Joint Research Centre, Environment Institute, TP280, I-21020 Ispra (Va), Italy. ⁶Max Planck Institute for Meteorology, Bundesstrasse 55, 20146 Hamburg, Germany. ⁷Naval Research Laboratory, Monterey, CA 93943, USA. ⁸Institute for Atmospheric Physics, German Aerospace Center (DLR), 82230 Wessling, Germany. ⁹Department of Geophysics and Planetary Science, Tel Aviv University, Ramat Aviv, 69978 Israel. ¹⁰Institute of Geophysics, Warsaw University, 02-093 Warsaw, Poland. ¹¹Environmental Chemical Processes Laboratory, University of Crete, 71409 Heraklion, Greece. ¹²Institute for Marine and Atmospheric Research, Utrecht University, 3584 CC Utrecht, Netherlands. ¹³Laboratory of Environmental and Climate Science, F-91191 Gif/Yvette Cedex, France. ¹⁴Royal Netherlands Meteorological Institute, Post Office Box 201, 3730 AE De Bilt, Netherlands. ¹⁵NOAA Aeronomy Laboratory, 325 Broadway R/AL7, Boulder, CO 80305, USA.

*To whom correspondence should be addressed. E-mail: lelieveld@mpch-mainz.mpg.de

40°N over the Atlantic Ocean and Europe, moving east with the mean flow and penetrating downward through a weak potential temperature gradient. In the boundary layer, on the other hand, where NO is only about 20 parts per trillion by volume, O₃ is destroyed (~2 ppbv/day). Chemistry transport model simulations (6, 12, 13) suggest that in the free troposphere, on average, 20 to 40% of the O₃ originates from the stratosphere. The rest is photochemically produced within the troposphere; about half of it is anthropogenic. In

the boundary layer, about 90% of the O₃ is formed in situ, with an anthropogenic fraction of about 75%.

Carbon monoxide pollution sources.

To further analyze the origin of pollutant gases, we focused on carbon monoxide (CO), for which we obtained good agreement between the measurements and a chemistry transport model (within ~10%) (13). The results of the model have been extensively tested, because it was also used for “chemical weather forecasting” during the project. The

model diagnoses CO from anthropogenic sources in different parts of Europe, North America, and Asia. From the trajectories in Fig. 1, we may expect that in the lower troposphere, emissions from western and eastern Europe would dominate. We performed model simulations for August 2001 over the western and eastern Mediterranean: over Sardinia (40°N, 8°E) and Crete (35°N, 25°E), respectively (Fig. 3). Considering the negligible influence of local pollution sources, the high CO levels, in excess of 150 ppbv,

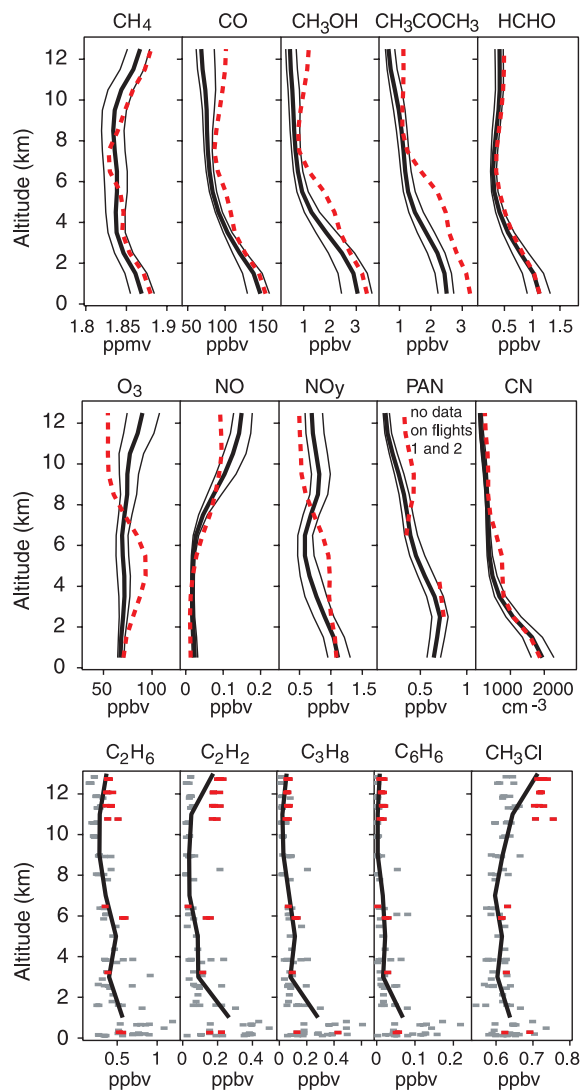
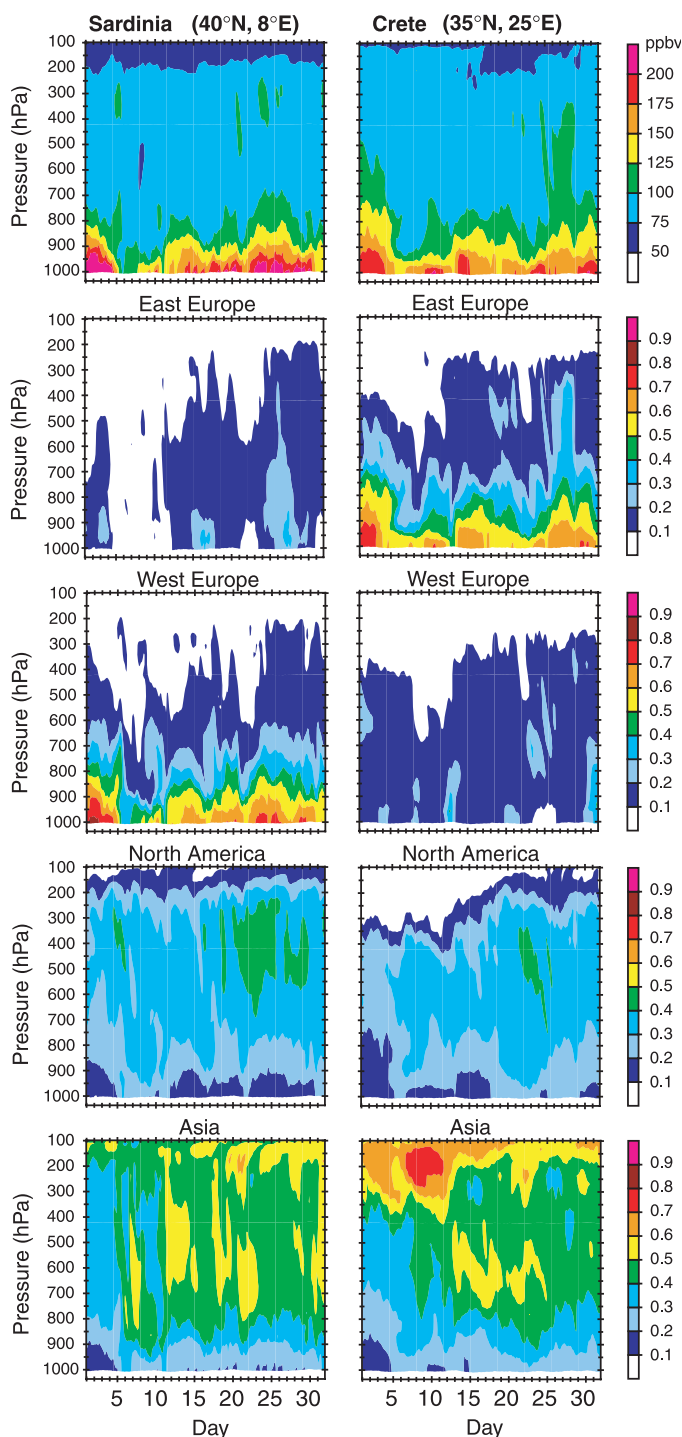


Fig. 2. (Left) Median vertical profiles (thick black lines), 1 σ standard deviations (thin black lines), and actual concentrations from canister samples (squares) obtained from 14 measurement flights in August 2001. The red dashed lines and squares present median and actual values, respectively, for the first three flights on 1, 3, and 8 August. During this week, the pollution from eastern Europe (lower 4 km), western Europe (4 to 6 km) and the southern Asian monsoon (>8 km) was particularly strong. ppmv, parts per million by volume. **Fig. 3. (Right)** CO tracer simulations, representing the western and eastern Mediterranean (left and right columns, respectively) during August 2001. The top panels show total CO; the other panels show fractional contributions from emissions in eastern Europe (>15°E), western Europe (<15°E), North America, and Asia.



are striking. In comparison, boundary-layer CO over the North Pacific in summer is typically about 60 to 70 ppbv, and over the relatively clean South Pacific this is only about 40 to 50 ppbv (14, 15), which is much lower than over the Mediterranean. The model results indicate that regions surrounding the Mediterranean such as southern Italy, Greece, Yugoslavia, the Middle East, and North Africa contribute relatively little to the CO pollution, typically about 20%.

The strongest influences over the western Mediterranean are from western Europe, notably France, Germany, and northern Italy. The eastern Mediterranean, on the other hand, is polluted by emissions from eastern Europe, in particular Poland, the Ukraine, and Russia. This pollution flow, east of the Carpathian Mountains, is channeled over the Black Sea, the Sea of Marmora, and the Aegean Sea. Consequently, long-range CO transport from both western and eastern Europe, mostly from fossil fuel use, contributes 60 to 80% of the boundary-layer CO over the Mediterranean. This range reflects the temporal CO changes associated with meteorological variability. The model results in Fig. 3 thus corroborate our aircraft measurements, showing that the entire Mediterranean lower troposphere is polluted, although the source regions differ markedly from west to east.

In the free troposphere where westerly winds prevail, the situation is quite different from the boundary layer. Middle tropospheric CO levels are about 75 to 80 ppbv, slightly higher than over the North Pacific in summer, where CO is typically 70 to 75 ppbv; whereas over the much cleaner South Pacific, the level is only about 50 ppbv (16, 17). The model tracer analysis shows that the largest contribution over the Mediterranean is from Asia (40 to 50%), in an extensive subtropical CO plume that combines with North American emissions (30 to 40%) before it crosses the Atlantic Ocean. In the middle troposphere,

the CO lifetime is about 1 to 2 months, which is comparable to the time in which an air mass circumnavigates the globe. Because CO at these altitudes is thus determined by very long range transport, its variability is relatively low (Figs. 2 and 3). The contributions by pollution from western and eastern Europe to middle tropospheric CO are only about 10%, except during the first week of August when these contributions were larger, up to about 25%. During this week, the lower 4 km of the troposphere was strongly affected by eastern European emissions, whereas at about 4 to 6 km we observed enhanced gaseous and particulate pollution from western Europe. These air masses carried large amounts of methanol and acetone, 2 to 3.5 ppbv (Fig. 2). The plume from western Europe at 4 to 6 km also contained much NO_y (all oxidized nitrogen excluding N_2O), associated with a strong O_3 increase.

An Asian plume near the tropopause.

In the upper troposphere, we distinguished another pollution layer with CO mixing ratios up to about 100 ppbv. Trajectory analysis and our model results suggest an important influence by Asian pollution from the east. Strongly enhanced pollution levels were observed, including relatively short-lived compounds (Fig. 2), especially along flight tracks over the eastern Mediterranean in early August. The Asian pollution contained relatively less nitrogen oxides and more acetylene (C_2H_2), peroxyacetyl nitrate (PAN), methyl cyanide (CH_3CN), and methyl chloride (CH_3Cl), indicating an important contribution from biomass burning, probably biofuel use, consistent with measurements made directly in the Asian outflow (18). Methane (CH_4) was also enhanced, possibly from rice cultivation. The measurements and model results furthermore suggest that the Asian pollution can also penetrate the lower stratosphere.

The remarkably strong influence of Asian pollution at the eastern Mediterranean tropopause is associated with Asian monsoon convection and the extended high-pressure trough in the upper troposphere. Anticyclonic

flow transports the pollution over Africa and subsequently northward, following the upper troposphere trajectories shown in Fig. 1. Isentropic transport across the subtropical tropopause can enhance CO in the middle latitude lower stratosphere in summer (19). Theoretical studies have predicted an important role for the Asian monsoon in troposphere-stratosphere transport, in particular at the west side of the upper troposphere anticyclone (20, 21). In summer, the tropopause over the Mediterranean slopes strongly downward toward the north, typically from an altitude of about 15 km over northern Africa to 11 km within about 5° latitude, associated with a relatively weak subtropical jet stream, high potential temperatures in the upper troposphere, and a weak cross-tropopause transport barrier. Back and forward trajectories from the upper troposphere region where we observed the high pollution levels, combined with ECMWF potential vorticity analysis, showed that there is an important link between the Asian monsoon, transport over the eastern Mediterranean, and pollution of the lower stratosphere at higher latitudes. This adds to stratospheric pollution by, for example, aircraft exhausts, which increases O_3 formation. Methyl chloride and other short-lived halocarbons in the Asian plume, however, have the opposite effect, because activation of chlorine and bromine radicals leads to O_3 destruction.

Ozone air quality. Deleterious effects of the observed pollution may be considerable. At the surface, mean O_3 mixing ratios are about 60 to 65 ppbv, reducing air quality. The stability of the Mediterranean troposphere, because of subsidence, suppresses entrainment from the free troposphere, another indication that the observed high O_3 in the boundary layer is formed in European air that is subsequently transported toward the Mediterranean. The pollution in reservoir layers between 1 and 4 km altitude also originates from Europe. These layers are formed at the northern Mediterranean coast, as residuals between the continental and marine boundary layer, and enhanced by land-sea breeze cir-

Table 1. Estimated enhancement factors for Mediterranean summer conditions compared to the Pacific background troposphere. Factors were obtained by dividing the MINOS median values by the range of values obtained from the literature for the central northern Pacific troposphere (14–17, 49–52). CN, condensation nuclei; FT, free troposphere; NO_x , $\text{NO} + \text{NO}_2$.

Species	Enhancement factor	
	BL	FT
CO	2–2.5	1–1.2
O_3	2.5–3	1.5–2
NO_x	2–4	2–3
PAN	20–100	5–7
CH_3COCH_3	5–6	2–5
CH_3OH	3–4	1.5–2.5
HCHO	4–5	3–5
CN	5–10	1.5–2

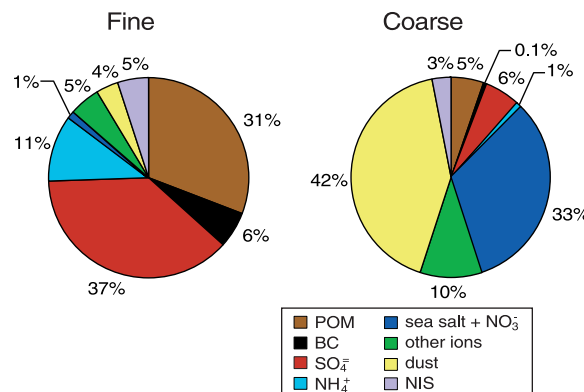


Fig. 4. Speciated mean aerosol mass in the fine (diameter $< 2 \mu\text{m}$) and coarse (diameter $> 2 \mu\text{m}$) particulate fraction during the MINOS campaign. The total fine aerosol mass is $16.6 \mu\text{g}/\text{m}^3$; the coarse aerosol mass is $24.2 \mu\text{g}/\text{m}^3$. Other ions include K^+ , Mg^{2+} , Ca^{2+} , and CO_3^{2-} . Sea salt includes about one-third nitrate. BC, black carbon; NIS, nonidentified species (such as fly ash).

culations and orographic flows (22). The measurements show that the variability of surface O_3 is relatively low (between 60 and 70 ppbv during the day, 1σ standard deviation ≈ 10 ppbv). The diurnal O_3 variation is small, only about 10%, with a minimum in the morning (~ 7 a.m.) and a maximum in the afternoon (1 to 3 p.m.). The regional background measurement station Finokalia, as well as a station in Malta ($36^\circ N$, $14^\circ E$), being predominantly under the influence of eastern and western European pollution sources, respectively, show very similar diurnal and seasonal O_3 cycles (4, 23, 24). This implies that in background air, the European 8-hourly air pollution standard of 55 ppbv is substantially exceeded throughout the Mediterranean region in summer. Ozone formation from local precursor emissions in urban and industrial areas along the Mediterranean coast adds to these already high background levels, so that strong air quality violations can occur in these areas (25).

Pollutant aerosol haze. At Finokalia, aerosols were measured nearly continuously, together with spectral optical depth and aerosol extinction, to determine the aerosol radiative forcing of climate (11, 26, 27). The resulting mean aerosol composition is shown (Fig. 4) for the fine and coarse particulate fractions, with a divide at particles of $2\text{-}\mu m$ diameter. Although southerly wind is uncommon in summer, Saharan dust outbreaks can still influence the Mediterranean through anticyclonic flow from western Africa, reaching the area from the west in the lower free troposphere. Although such events only occur occasionally, they can significantly affect the mean coarse aerosol fraction (28–31). The coarse particles also carry substantial amounts of inorganic ions, in particular ammonium bisulfate and nitrate, the latter associated with sea salt. The fine aerosol fraction contains most ammonium bisulfate, on average about $8\text{ }\mu g/m^3$. Previous studies have

shown that only a small part, about 5 to 25%, of the sulfate originates from natural sources; i.e., from dimethyl sulfide emissions by the ocean (27, 28). Ammonium is also largely anthropogenic (27), and it strongly correlates with sulfate ($r^2 \approx 0.8$). The contribution of black carbon is about 6%, and it does not have natural sources at all. This 6% may not seem large; however, it does have an important influence on the aerosol radiative forcing (32). Particulate organic matter (POM) is mostly found in the fine aerosol fraction, typically contributing about $5\text{ }\mu g/m^3$. Only a small part of the POM, up to about $0.2\text{ }\mu g/m^3$, appears to be related to biogenic emissions (formate, acetate, and $\geq C_9$ compounds), so POM is also largely anthropogenic. Hence about 80 to 90% of the fine aerosol fraction, which is optically most active, originates from nonnatural sources. The coarse fraction, on the other hand, is probably about 60 to 80% natural.

Radiative forcing of climate. The radiation measurements at Finokalia show a mean aerosol optical depth at 500 nm (AOD_{500}) of 0.21 during clear sky conditions, which is slightly lower than Aerosol Robotic Network (AERONET) measurements at coastal locations and in agreement with previous measurements in the region (9, 10, 33). The mean aerosol single-scatter albedo was 0.87. By taking the difference between the average conditions and conditions during one relatively clean day (AOD_{500} of 0.06), we calculated the aerosol radiative forcing using the method of Ramanathan *et al.* (32).

We compared the results with greenhouse gas (GHG) forcing calculations, based on trace gas profiles during MINOS and model-calculated profiles, by assuming natural emissions only (Fig. 5). We emphasize that the results of the GHG forcing calculations have global significance, whereas the aerosol forcing is regional (and seasonal), associated with the much shorter aerosol lifetime. A remarkable result is the large diurnal mean surface forcing, about 18 W m^{-2} , being a factor of 2.7 larger than the top-of-the-atmosphere (TOA) forcing (34, 35). The difference is caused by solar radiation absorption by black carbon, water vapor, and possibly also by dust, fly ash, and organic carbon, thus causing an atmospheric forcing of more than 11 W m^{-2} . Because much of this atmospheric forcing is exerted in the lower 4 km, it is likely that the warming tendency is exported to northern Africa with the mean flow. The large reduction in surface solar radiation by aerosols is similar to that observed over the northern Indian Ocean in the Asian pollution outflow (32).

Perturbation of the hydrological cycle.

The large seasonal variation in Mediterranean sea surface temperature (SST) of about $11^\circ C$, in response to solar heating (2), suggests considerable sensitivity to the aerosol surface forcing. Longterm SST variability, on the other hand, is related to the Mediterranean Oscillation, modulated by the North Atlantic Oscillation (1, 2, 36). SST variability was relatively regular during the first several decades after 1930. In the 1970s, however, substantial cooling took place, followed by an extensive warming period. The temperature tendencies during the past three decades correlate with European sulfur dioxide (SO_2), with highest emissions (and thus sulfate) coincident with lowest SSTs in the late 1970s (Fig. 6). A recent analysis of the surface energy budget and satellite measurements confirms that the solar energy input into the Mediterranean Sea has been reduced by about 25 W m^{-2} , suggesting a large effect on the thermohaline circulation (37). Another likely consequence of the aerosol surface cooling is a reduction of evaporation and precipitation. Maracchi *et al.* (38) derived a direct relationship between the SST and precipitation events in Italy, concluding that a $1.8^\circ C$ change causes precipitation anomalies of 40 to 65%.

To evaluate possible effects on the hydrological cycle, we forced a climate model with maximum and minimum monthly mean observed Mediterranean SSTs (39–42). The results of these sensitivity simulations, which likely yield an upper limit of the aerosol surface cooling effect during the past decades, indicate large precipitation reductions of 10 to 50% in the Mediterranean region, the Middle East, and the eastern Sahel (Fig. 7). The model-calculated changes largely result

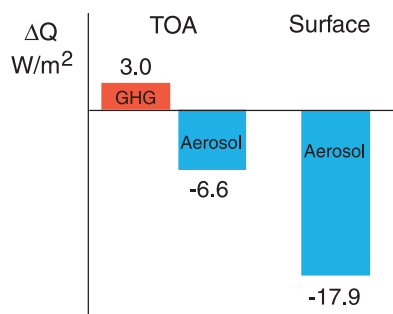


Fig. 5. Diurnal, mean, clear-sky radiative forcing (ΔQ) over the Mediterranean in summer at the top of the atmosphere and at the ocean surface, calculated from aerosol, GHG, and radiation measurements. The GHG effect represents the long-wave forcing (by infrared radiation absorption), whereas aerosols affect the radiation budget through solar radiation extinction.

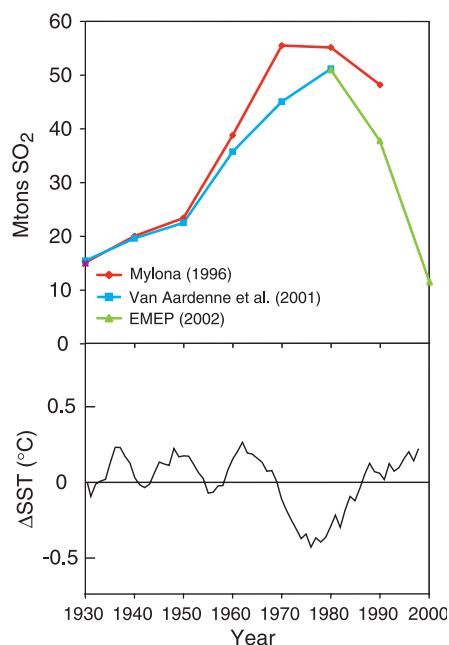
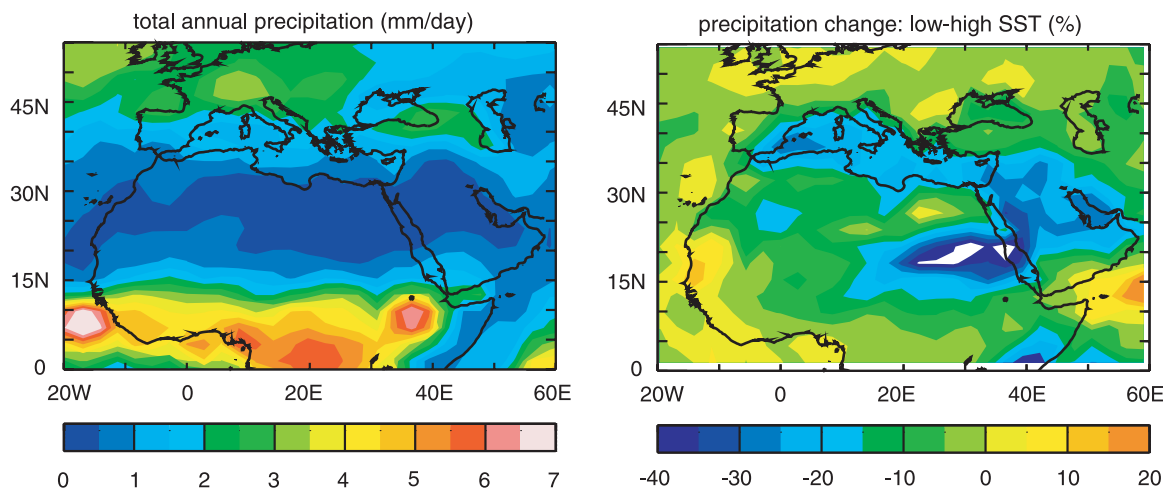


Fig. 6. (Top) Estimated European SO_2 emissions (46, 53, 54). (Bottom) Five-year running mean of annual Mediterranean SST anomalies (42). Mtons, megatons; ΔSST , change in sea surface temperature.

Fig. 7. Mean results from 10-year model simulations (39). **(Left)** Total annual average precipitation in the Mediterranean and nearby regions. **(Right)** Percentage changes in annual precipitation as boundary conditions in the model using observed low and high Mediterranean SSTs.



from convective precipitation decreases. Consistently, Nicholson *et al.* (43) report strong rainfall reductions in the eastern Sahel, in particular in the 1970s and 1980s, coincident with the maximum sulfate forcing. Droughts in the western Sahel, on the other hand, are probably related to changes in the western African monsoon intensity, driven by the tropical Atlantic SST (44). Anomalous dryness was especially severe in summer, with a maximum in August, which normally brings most precipitation. In the eastern Sahel, rainfall conditions improved again during the 1990s (43), together with decreasing European SO₂ emissions and consistent with a negative sulfate aerosol trend (27–31) and with reduced sulfate deposition in Hungary, Italy, southern France, and Spain since 1980 (45, 46). Although the aerosol forcing is largest in summer, the delayed ocean response conveys the effect into the autumn and winter, when precipitation is strongest directly around the Mediterranean. Our model calculations do not account for rain suppression by aerosols, which may play a role as well (47, 48). It should furthermore be mentioned that the increasing SSTs since 1980 are probably not only a consequence of the reduced sulfate forcing but also of a growing global warming influence. These results underscore the importance of accounting for both aerosol and GHG trends in transient climate simulations.

Air quality and climate. We conclude that European pollution of the Mediterranean lower troposphere strongly reduces air quality, particularly during summer. Our model study suggests that it also substantially affects climate and the hydrological cycle. In the free troposphere, pollution is largely determined by intercontinental transport, whereas upper tropospheric pollution from Asia can reach the stratosphere. These “cross-roads” carry large pollution loads over the Mediterranean, and the negative effects extend far beyond the region. International

efforts are called for to reduce these atmospheric environmental stresses and to further investigate the links between Mediterranean and global climate change.

References and Notes

1. J. P. Palutikof, M. Conte, J. Casimiro Mendes, C. M. Goodess, F. Espirito Santo, in *Mediterranean Desertification and Land Use*, C. J. Brandt, J. B. Thornes, Eds. (Wiley, Chichester, UK, 1996), pp. 43–86.
2. H.-J. Bolle, Ed., *Mediterranean Climate: Variability and Trends* (Springer-Verlag, Berlin, 2002).
3. M. Millán, R. Salvador, E. Mantilla, G. Kallos, *J. Appl. Meteorol.* **4**, 487 (2000).
4. G. Kouvarakis, K. Tsigaridis, M. Kanakidou, N. Mihalopoulos, *J. Geophys. Res.* **105**, 4399 (2000).
5. M. G. Lawrence, P. J. Crutzen, P. J. Rasch, B. E. Eaton, N. M. Mahowald, *J. Geophys. Res.* **104**, 26245 (1999).
6. J. Lelieveld, F. J. Dentener, *J. Geophys. Res.* **105**, 3531 (2000).
7. D. A. Hauglustaine, G. P. Brasseur, *J. Geophys. Res.* **106**, 32337 (2001).
8. J. Haywood, O. Boucher, *Rev. Geophys.* **38**, 513 (2000).
9. P. Formenti *et al.*, *J. Geophys. Res.* **106**, 9807 (2001).
10. T. W. Andreae *et al.*, *J. Geophys. Res.* **107**, 10.1029/2001JD900252 (2002).
11. The MINOS home page at www.mpch-mainz.mpg.de/~reus/ offers background information; project objectives; descriptions of measurement platforms and instrumentation; meteorological information, including back-trajectories; participating institutions; contact persons; and modeling results.
12. G. J. Roelofs, J. Lelieveld, *J. Geophys. Res.* **105**, 22697 (2000).
13. Model details are offered at www.mpch-mainz.mpg.de/~lawrence/MATCH/match_overview.html. Chemical weather forecasts to support campaign planning are presented through the MINOS home page (11) and at www.mpch-mainz.mpg.de/~lawrence/forecasts.html. The mean correlation coefficient between measured and modeled CO along the flight tracks is $r = 0.73$. The addition of non-methane hydrocarbon emissions to the model (5) and their CO yield are described at www.mpch-mainz.mpg.de/~kuhlmann/rvkdisshtml/.
14. P. C. Novelli, K. A. Masari, P. M. Lang, *J. Geophys. Res.* **103**, 19015 (1998).
15. V. Gros, B. Bonsang, D. Martin, P. C. Novelli, V. Kazan, *Chemosphere Global Change Sci.* **1**, 163 (1999).
16. M. G. Schultz *et al.*, *J. Geophys. Res.* **104**, 5829 (1999).
17. E. V. Browell *et al.*, *J. Geophys. Res.* **106**, 32481 (2001).
18. J. Lelieveld *et al.*, *Science* **291**, 1031 (2001).
19. P. Hoor *et al.*, *J. Geophys. Res.* **107**, 10.1029/2000JD000289 (2002).
20. P. Chen, *J. Geophys. Res.* **100**, 16661 (1995).
21. A. Dethof, A. O'Neill, J. Slingo, *J. Geophys. Res.* **105**, 12279 (2000).
22. M. Millán, R. Salvador, E. Mantilla, G. Kallos, *J. Geophys. Res.* **102**, 8811 (1997).
23. G. Kouvarakis *et al.*, *J. Geophys. Res.* **107**, 10.1029/2000JD000081 (2002).
24. M. Nolle, R. Ellul, G. Heinrich, H. Güsten, *Atmos. Environ.* **36**, 1391 (2002).
25. G. Gangioti, M. M. Millán, R. Salvador, E. Mantilla, *Atmos. Environ.* **35** (2001).
26. The aerosol sampling and analysis techniques are described in (27) and (29). Non-sea salt sulfate concentrations at Finokalia ($\approx 6 \mu\text{g}/\text{m}^3$) are somewhat lower than along the Mediterranean coast north and east of Crete ($\approx 10 \mu\text{g}/\text{m}^3$), as shown in (9) and (27–31).
27. N. Mihalopoulos, E. Stephanou, M. Kanakidou, S. Pilitsidis, P. Bousquet, *Tellus* **49B**, 314 (1997).
28. E. Ganor, H. A. Foner, H. G. Bingemer, R. Udisti, I. Setter, *Atmos. Environ.* **34**, 3453 (2000).
29. G. Kouvarakis *et al.*, *J. Geophys. Res.* **107**, 10.1029/2000JD000291 (2002).
30. M. Luria *et al.*, *J. Geophys. Res.* **101**, 25917 (1996).
31. T. Özsoy, C. Saydam, N. Kubilay, I. Salihoglu, *Global Atmos. Ocean Syst.* **7**, 185 (2000).
32. V. Ramanathan *et al.*, *J. Geophys. Res.* **106**, 28371 (2001).
33. See the AERONET Web site at <http://aeronet.gsfc.nasa.gov/>.
34. K. M. Markowicz, P. J. Flatau, M. V. Ramana, P. J. Crutzen, V. Ramanathan, *Geophys. Res. Lett.* **29**, 10.1029/2002GL015767 (2002). The TOA forcing for aerosols that absorb solar radiation switches from negative values in clear-sky conditions to positive values at a cloud cover of about 25% (35). The values presented here are for clear skies over Finokalia. The neglect of clouds, though they are scarce in summer (<15%), introduces an uncertainty range of $\pm 2.4 \text{ W m}^{-2}$.
35. V. Ramanathan, P. J. Crutzen, J. T. Kiehl, D. Rosenfeld, *Science* **294**, 2119 (2001).
36. P. Maheras, E. Xoplaki, H. Kutiel, *Theor. Appl. Clim.* **64**, 189 (1999).
37. E. Tragou, A. Lascaratos, *J. Geophys. Res.*, in press.
38. G. Maracchi, A. Crisci, B. Gozzini, F. Meneguzzo, G. Zipoli, paper presented at the 3rd European Conference on Applied Climatology, Pisa, Italy, 16 to 20 October 2000.
39. We applied the European Centre model, Hamburg version 4 (ECHAM-4), described in (40) and (41), at T42 resolution (about 2.8° latitude-longitude). The model was forced with SSTs of the Mediterranean and Black Sea (42) and used observed maximum and minimum monthly mean values. The seasonal SST amplitude was 14° to 15.5°C in February to 24.5° to 27°C in August. These sensitivity calculations do not account for changes in atmospheric heating gradients by aerosol absorption or indirect aerosol influences on clouds, which could additionally impose strong climate forcings, including a suppression of moisture

- transport (32). The model was also used for tracer forecasts during the MINOS campaign.
40. E. Roeckner *et al.* "The atmospheric general circulation model ECHAM-4: Model description and simulation of present-day climate," *MPI-Report 218* (Max Planck Institute for Meteorology, Hamburg, Germany, 1996).
41. E. Roeckner, L. Bengtsson, J. Feichter, J. Lelieveld, H. Rodhe, *J. Clim.* **12**, 3004 (1999).
42. N. A. Rayner, E. B. Horton, D. E. Parker, C. K. Folland, R. B. Hackett, Version 2.2 of the Global Sea-Ice and Sea Surface Temperature Data Set, 1903–1994, Climate Research Technical Note 74 (Hadley Centre, Bracknell, UK, 1996); available at www.met-office.gov.uk/research/hadleycentre/obsdata/GISST.html.
43. S. Nicholson, S. Some, B. Kone, *J. Clim.* **13**, 2628 (2000).
44. D. P. Rowell, C. K. Folland, K. Maskell, M. L. Ward, Q. J. *Meteorol. Soc.* **121**, 669 (1995).
45. A. Avila, F. Rodà, *Atmos. Environ.* **36**, 2881 (2002).
46. The Programme for Monitoring and Evaluation of the Long-Range Transmission of Air Pollutants in Europe (EMEP), at www.emep.int, offers estimates of emissions variable over time (since 1980) of European anthropogenic trace species.
47. D. Rosenfeld, *Science* **287**, 1793 (2000).
48. L. D. Rotstayn, U. Lohmann, *J. Clim.*, **15**, 2103 (2002).
49. A. S. Board *et al.*, *J. Geophys. Res.* **104**, 16181 (1999).
50. A. D. Clarke *et al.*, *J. Geophys. Res.* **106**, 32555 (2001).
51. H. Singh *et al.*, *Nature* **410**, 1078 (2001).
52. J. Sciare, E. Baboukas, N. Mihalopoulos, *J. Atmos. Chem.* **39**, 281 (2001).
53. S. Mylona, *Tellus* **48B**, 662 (1996).
54. J. van Aardenne, F. J. Dentener, J. G. J. Olivier, C. G. M. Klein Goldewijk, J. Lelieveld, *Global Biogeochem. Cycles* **15**, 909 (2001). The SO₂ emission estimates are inherently uncertain. The SO₂ decrease after 1980 is nevertheless consistent with sulfate concentration and deposition data (27–31, 45, 46).
55. Funding from the NSF contributed to this work. The King Air flights were supported by the Israeli Space Agency as part of the Mediterranean Israeli Dust Experiment (MEIDEX).

25 June 2002; accepted 17 September 2002

Transcriptional Regulatory Networks in *Saccharomyces cerevisiae*

Tong Ihn Lee,^{1*} Nicola J. Rinaldi,^{1,2*} François Robert,^{1*} Duncan T. Odom,¹ Ziv Bar-Joseph,³ Georg K. Gerber,³ Nancy M. Hannett,¹ Christopher T. Harbison,^{1,2} Craig M. Thompson,^{1†} Itamar Simon,¹ Julia Zeitlinger,¹ Ezra G. Jennings,^{1,2} Heather L. Murray,¹ D. Benjamin Gordon,¹ Bing Ren,^{1‡} John J. Wyrick,^{1§} Jean-Bosco Tagne,¹ Thomas L. Volkert,¹ Ernest Fraenkel,¹ David K. Gifford,³ Richard A. Young^{1,2||}

We have determined how most of the transcriptional regulators encoded in the eukaryote *Saccharomyces cerevisiae* associate with genes across the genome in living cells. Just as maps of metabolic networks describe the potential pathways that may be used by a cell to accomplish metabolic processes, this network of regulator-gene interactions describes potential pathways yeast cells can use to regulate global gene expression programs. We use this information to identify network motifs, the simplest units of network architecture, and demonstrate that an automated process can use motifs to assemble a transcriptional regulatory network structure. Our results reveal that eukaryotic cellular functions are highly connected through networks of transcriptional regulators that regulate other transcriptional regulators.

Genome sequences specify the gene expression programs that produce living cells, but how cells control global gene expression programs is far from understood. Each cell is the product of specific gene expression programs involving regulated transcription of thousands of genes. These transcriptional programs are modified as

cells progress through the cell cycle, in response to changes in environment, and during organismal development (1–5).

Gene expression programs depend on recognition of specific promoter sequences by transcriptional regulatory proteins (6–9). Because these regulatory proteins recruit and regulate chromatin-modifying complexes and components of the transcription apparatus, knowledge of the sites bound by all the transcriptional regulators encoded in a genome can provide the information necessary to nucleate models for transcriptional regulatory networks. With the availability of complete genome sequences and development of a method for genome-wide binding analysis (also known as genome-wide location analysis), investigators can identify the set of target genes bound in vivo by each of the transcriptional regulators that are encoded in a cell's genome. This approach has been used to identify the

genomic sites bound by nearly a dozen regulators of transcription (10–13) and several regulators of DNA synthesis (14) in yeast.

Experimental design. We used genome-wide location analysis to investigate how yeast transcriptional regulators bind to promoter sequences across the genome (Fig. 1A). All 141 transcription factors listed in the Yeast Proteome Database (15) and reported to have DNA binding and transcriptional activity were selected for study. Yeast strains were constructed so that each of the transcription factors contained a myc epitope tag. To increase the likelihood that tagged factors were expressed at physiologic levels, we introduced epitope tag coding sequences into the genomic sequences encoding the COOH terminus of each regulator, as described in (16). We confirmed appropriate insertion of the tag and expression of the tagged protein by polymerase chain reaction and immunoblot analysis. Introduction of an epitope tag might be expected to affect the function of some transcriptional regulators; for 17 of the 141 factors, we were not able to obtain viable tagged cells, despite three attempts to tag each regulator. Not all the transcriptional regulators were expected to be expressed at detectable levels when yeast cells were grown in rich medium, but immunoblot analysis showed that 106 of the 124 tagged regulator proteins could be detected under these conditions.

We performed a genome-wide location analysis experiment (10) for each of the 106 yeast strains that expressed epitope-tagged regulators (17, 18). Each tagged strain was grown in three independent cultures in rich medium (yeast extract, peptone, dextrose). Genome-wide location data were subjected to quality control filters and normalized, and the ratio of immunoprecipitated to control DNA was determined for each array spot. We calculated a confidence value (*P* value) for each spot from each array by using an error model (19). The data for each of the three samples in an experiment were combined by a weighted average method (19); each ratio was weighted by *P* value and then averaged. Final *P* values for these combined ratios were then calculated (17, 18).

Given the properties of the biological sys-

¹Whitehead Institute for Biomedical Research, Nine Cambridge Center, Cambridge, MA 02142, USA. ²Department of Biology, Massachusetts Institute of Technology, Cambridge, MA 02139, USA. ³MIT Laboratory of Computer Science, 200 Technology Square, Cambridge, MA 02139, USA.

*These authors contributed equally to this work.

†Present address: Akceli Inc., 1 Hampshire Street, Cambridge, MA 02139, USA.

‡Present address: Ludwig Institute for Cancer Research, 9500 Gilman Drive, La Jolla, CA 92093, USA.

§Present address: California Institute of Technology, Pasadena, CA 91125, USA.

||To whom correspondence should be addressed. E-mail: young@wi.mit.edu